Research Article

Nano Research
2023, 16(1): 1726–1732

ISSN 1998-0124 CN 11-5974/O4
https://doi.org/10.1007/s12274-022-4772-x

Construction of hollow mesoporous $ZnMn_2O_4$/C microspheres with carbon nanotubes embedded in shells for high-performance aqueous zinc ions batteries

Feiran Chen[1], Qinru Wang[1], Xiaofeng Yang[1], Chao Wang[1], Hu Zang[1], Yingwen Tang[2], Tao Li[3], and Baoyou Geng[1,4] (✉)

[1] *College of Chemistry and Materials Science, the Key Laboratory of Electrochemical Clean Energy of Anhui Higher Education Institutes, Anhui Provincial Engineering Laboratory for New-Energy Vehicle Battery Energy-Storage Materials, Anhui Normal University, Wuhu 241002, China*
[2] *College of Physics and Information Engineering, Minnan Normal University, Zhangzhou 363000, China*
[3] *Shanghai Institute of Technical Physics, Chinese Academy of Sciences, Shanghai 100029, China*
[4] *Institute of Energy, Hefei Comprehensive National Science Center, Hefei 230031, China*

Received: 29 June 2022 / **Revised:** 10 July 2022 / **Accepted:** 13 July 2022

ABSTRACT

Recently, rechargeable zinc-ion batteries have been considered as the future development direction of large-scale energy storage due to their low price, safety, environmental friendliness, and excellent electrochemical performance. However, high-capacity, long-cycle stable cathode materials that can meet the demand are still to be developed. Herein, the hollow mesoporous $ZnMn_2O_4$/C microsphere cathode material with carbon nanotubes embedded in the shell was prepared by spray pyrolysis for the first time. Its capacity remained at 209.71 mAh·g^{-1} after 150 cycles at a rate of 0.5 A·g^{-1}, and still maintained a specific capacity of 100.06 mAh·g^{-1} at a rate of 1 A·g^{-1} after 1,000 cycles. The outstanding performance is attributed to the hollow structure that can effectively buffer large volume changes caused by ion intercalation and deintercalation, excellent porosity, cationic defects, and high electrical conductivity of carbon nanotubes and its strong adsorption to $ZnMn_2O_4$ nanoparticles.

KEYWORDS

mesoporous hollow microspheres, carbon nanotubes, zinc-ion battery, $ZnMn_2O_4$

1 Introduction

Among the ion-based batteries, lithium-ion (Li-ion) batteries have been widely used and studied, and their characteristics, such as high energy density and excellent lifetime, are considered to be the most promising option [1, 2]. However, due to the scarcity of lithium resources, environmental pollution, and low safety, the large-scale application of lithium-ion batteries still faces serious problems [3, 4]. Rechargeable aqueous zinc-ion batteries (AZIBs) have attracted much attention due to their dual electron transfer mechanism, nontoxicity, low redox potential (−0.76 V vs. SHE), and high theoretical capacity (820 mAh·g^{-1}) of zinc electrodes [5–11]. It will be one of the candidates for large-scale energy storage in the future. However, commonly used manganese-based cathode materials dissolve rapidly during cycling resulting in rapid capacity decay, while vanadium-based materials cannot provide high energy density despite their excellent cycling stability. Therefore, it is urgent to develop the cathode materials with both high specific capacity and cycling stability for AZIBs [12–16].

Notably, the spinel-structured $ZnMn_2O_4$ (ZMO) is a potential high-efficiency cathode material for AZIBs due to its high redox potential, low cost, and abundant raw materials [17–20]. To solve the problem of capacity fading during cycling, many methods have been proposed, among which the addition of carbon materials has become one of the most important methods. Carbon nanotubes (CNTs) have a large specific surface area and pore structure, and their composite structure has excellent electrical conductivity, which can provide sufficient electrolyte channels, and has become an ideal candidate carbon material [21–24]. For example, Liu et al. synthesized α-MnO_2 nanofibers/carbon nanotubes hierarchically assembled microsphere materials, in which α-MnO_2 uniformly anchored on the CNTs-based framework showed a significantly increased tap density, effectively improving the electrochemical stability. The highest areal energy density of the material at 0.2 A·g^{-1} is 0.98 Wh·cm^{-2} [25]. Moreover, the hollow spherical structure is a promising buffer for large volume changes induced by ion intercalation and deintercalation [26–28]. Wu et al. used solvothermal carbon templates to prepare hollow porous ZMO materials. Due to the hollow porous structure and defects of the material, excellent zinc storage properties were created. The material exhibits a reversible discharge capacity of 106.5 mAh·g^{-1} after 300 cycles at 0.1 A·g^{-1} [19]. And compared to nanomaterials, microscale materials have high tap density [29]. Therefore, it is an effective strategy to improve the stability of this carbon composite during cycling by constructing a hollow microsphere structure.

Herein, we propose a simple and efficient method to embed carbon nanotubes (CNTs) in the shell of $ZnMn_2O_4$/C hollow

Address correspondence to bygeng@mail.ahnu.edu.cn

mesoporous microspheres (ZMO-CNT/C) with excellent zinc storage properties by spray pyrolysis. The hollow mesoporous microsphere structure effectively buffers the large volume change caused by the intercalation of zinc ions and provides a large specific surface area and abundant pore structure. ZMO nanoparticles are anchored to carbon nanotubes, which greatly improves the electrochemical stability and electrical conductivity. The sample ZMO-CNT/C retains a specific capacity of 209.71 mAh·g^{-1} after 150 cycles at 0.5 A·g^{-1} and 100.06 mAh·g^{-1} after 1,000 cycles at a high current density of 1 A·g^{-1}. This unique composite structure has a potential for the improvement of rechargeable AZIBs.

2 Experimental section

2.1 Materials

All materials were purchased commercially without further purification. Manganese sulfate monohydrate (AR), zinc nitrate hexahydrate (AR), and polyvinylpyrrolidone (PVP, K30, GR) were bought from Sinopharm Reagent Co., Ltd. Carboxylated multi-walled carbon nanotubes, polyvinylidene fluoride (PVDF, AR) and N,N-dimethylformamide (DMF, electronic grade) were obtained from Aladdin Reagent Co., Ltd. 98% zinc trifluoromethanesulfonate, and 50% manganese nitrate solution (AR) were purchased from Macleans Reagent Co., Ltd. Conductive carbon black (battery grade), zinc sheet (battery grade), flexible graphite paper (1 mm), gasket (battery grade), spring sheet (battery grade), battery case 2032 (battery grade), and Whatman GF/D Glass Fiber Filter Paper were bought from Nanjing Morges Co., Ltd.

Synthesis of $ZnMn_2O_4$-CNT/C. First, 20 mg of carboxylated multi-walled carbon nanotubes were dissolved in 20 mL of deionized water. A mixed solution with uniform dispersion was obtained after sonication for 25 min. Next, 0.25 g of PVP was added to the mixed solution, and it was completely dissolved by ultrasonication for 45 min. Then, 0.8312 g of zinc nitrate hexahydrate and 2 g of 50% manganese nitrate solution were added under stirring and stirred for 40 min to obtain the precursor solution for spraying. The mixed solution was ultrasonically atomized, and the atomized particles were treated at a high temperature in a 500 °C tube furnace. The obtained powder samples were then dried in a vacuum drying oven at 60 °C for 14 h to obtain the final product $ZnMn_2O_4$-CNT/C.

Synthesis of $ZnMn_2O_4$/C. The synthesis process of $ZnMn_2O_4$/C was similar to that of $ZnMn_2O_4$-CNT/C, except that no carbon nanotubes were added to the precursor solution (the obtained product was labeled as ZMO/C).

Synthesis of $ZnMn_2O_4$-CNT/C-400. 0.1 g of the prepared $ZnMn_2O_4$-CNT/C was calcined in a muffle furnace at a heating rate of 2 °C·min^{-1} for 2 h at 400 °C to obtain $ZnMn_2O_4$-CNT/C-400 (ZMO-CNT/C-400).

Synthesis of $ZnMn_2O_4$-CNT/C-500. The preparation method was the same as that of $ZnMn_2O_4$-CNT/C-400, except that the calcination temperature was 500 °C, and the product was named as ZMO-CNT/C-500.

2.2 Material characterization

We performed phase analysis of the material at 10°–80° by powder X-ray diffractometer (PXRD, Bruker AXS, D8 Advance). The chemical environment of the material surface was analyzed by X-ray photoelectron spectroscopy (XPS, Thermo Fisher, ESCALAB 250XI). The morphology and structure of the products were evaluated by high-resolution transmission electron microscopy (HRTEM), TEM, and scanning electron microscopy (SEM) on FEI, Talos F200x, Hitachi, HT-7700, and Hitachi, S-8100. Thermogravimetric analyzer tested by TA, Q500 analyzer in air from 20–800 °C. The specific surface area and pore size distribution were tested through Brunner–Emmett–Teller (BET, McMurray ASAP2010N) and Barrett–Joyner–Halenda (BJH) using N_2 adsorption isotherm. The ion content was detected by inductively coupled plasma optical emission spectrometry (ICP-OES, Agilent-5110).

2.3 Electrochemical measurements

The test batteries were 2032 type zinc-ion batteries assembled at room temperature. When preparing the battery, the electrode material, conductive carbon black, and PVDF were ground and mixed in a mass ratio of 7:2:1, an appropriate amount of N-methyl pyrrolidone (NMP) was added thereto, and then the obtained slurry was coated on flexible graphite paper. After drying in a vacuum drying oven at 60 °C for 12 h, the flexible graphite paper was cut into circular electrode sheets for battery assembly. In addition, the active material mass loading of the electrodes was in the range of 1.0–1.3 mg·cm^{-2}. We used deionized water composed of 2 M zinc trifluoromethanesulfonate and 0.1 M $MnSO_4$ as the electrolyte during assembly. Whatman GF/D glass fiber filter paper was used as the separator. The battery performance was tested in a battery test system (Neware, CT-4008) at 0.8 to 1.9 V. The cyclic voltammetry (CV) curves were obtained in the potential window range of 0.8–1.9 V on the CHI 660E electrochemical workstation, and alternating current (AC) impedance measurements were simultaneously performed on the same workstation with 0.01 V amplitude from 0.1 MHz to 0.01 Hz.

3 Results and discussion

Scheme 1 shows the synthesis process of ZMO-CNT/C. First, a certain molar ratio of Zn^{2+}, Mn^{2+}, and an appropriate amount of CNT and PVP were dissolved in a beaker in sequence. Then, the precursor solution was subjected to spray pyrolysis in a tube furnace at a set temperature, and ZMO-CNT/C hollow mesoporous composite microspheres were obtained after drying.

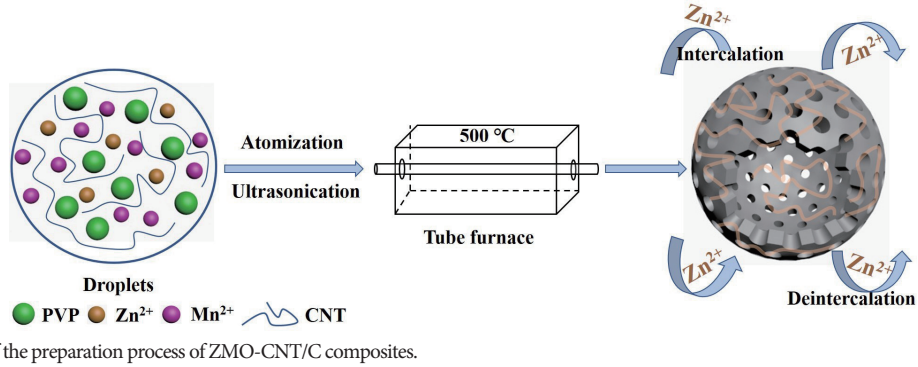

Scheme 1 Schematic of the preparation process of ZMO-CNT/C composites.

The composition of products was characterized by X-ray diffraction, as shown in Fig. S1 in the Electronic Supplementary Material (ESM). The diffraction peaks of ZMO-CNT/C, ZMO/C, ZMO-CNT/C-400, and ZMO-CNT/C-500 match well with the standard peaks of body-centered tetragonal $ZnMn_2O_4$ (PDF#77-0470). By comparison, it was found that the intensity of the diffraction peaks increased after calcination, but no other impurity peaks appeared, indicating that the sample was of high purity. To evaluate the carbon content in ZMO-CNT/C and ZMO/C, thermo gravity analysis (TGA) was performed. It can be seen from Fig. S2 in the ESM that the carbon content in ZMO/C is 2.7%, while that in ZMO-CNT/C is 3.7%, and the increased carbon content comes from the carbon nanotubes in the latter.

To further analyze the chemical states of surface elements, we performed XPS characterization on the ZMO-CNT/C. Characteristic peaks of Zn 2p, Mn 2p, C 1s, N 1s, and O 1s can be observed from the overall spectrum in Fig. 1. Figure 1(b) shows the high-resolution XPS spectra of Zn 2p, the characteristic peaks at 1,021.41 and 1,044.50 eV correspond to Zn $2p_{3/2}$ and Zn $2p_{1/2}$. Figure 1(c) shows the high-resolution XPS spectra of Mn 2p, two typical peaks appear at 641.93 and 653.88 eV, corresponding to Mn $2p_{3/2}$ and Mn $2p_{1/2}$. The fitting of the deconvolution peaks shows that there are Mn(III) and Mn(IV) in the sample. According to the area ratio of each valence state, the average Mn valence state is calculated to be 3.48, which is similar to the previous report, indicating the existence of Mn vacancies [30].

To illustrate the existence of Mn vacancies, the ZMO-CNT/C was tested by ICP measurement, and the ratio of Zn to Mn was 1:1.67. Therefore, the existence of Mn vacancies in spinel can be jointly verified from the fact that manganese has a valence higher than the standard trivalent, and the ratio of Mn:Zn in the sample is lower than the stoichiometric number 2. In the C 1s spectra of Fig. 1(d), the characteristic peaks at 284.73, 285.89, 286.49, and 288.39 eV correspond to the C=C/C–C, C–O, C–O–Mn, and C=N/C=O, respectively [20, 31]. Figure 1(e) shows the high-resolution N 1s spectra, in which the peaks at 398.49 and 399.93 eV correspond to pyridine nitrogen and pyridine nitrogen, respectively. Obviously, the content of pyridine nitrogen is higher, which can increase the conductivity and generate more defects. While the peaks located at 401.69 and 402.01 eV match graphitized nitrogen and oxynitride [32]. The XPS spectra of O 1s are shown in Fig. 1(f), in which the highest peak at 530.08 eV corresponds to a typical metallic O bond, while the peaks at 531.38 and 532.43 eV represent Mn–OH and H–O–H, indicating the existence of defects in the material [33].

Figure 2 shows the SEM and TEM images of the sample ZMO-CNT/C at different magnifications. Figure 2(a) shows that the product ZMO-CNT/C is a smooth-surfaced sphere with a diameter of about 1–2 μm, and some CNTs can be clearly seen wrapped around the surface of the sphere. And no CNTs

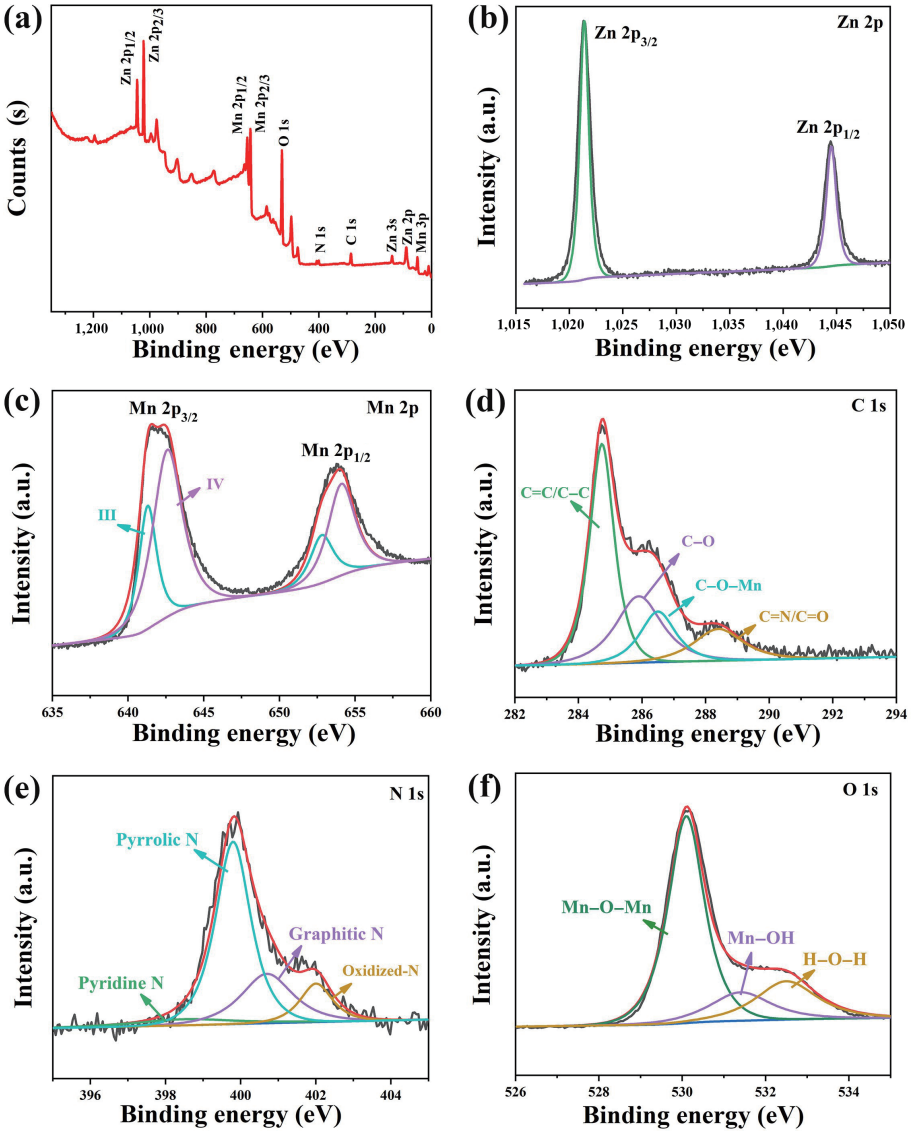

Figure 1 (a) XPS spectrum of the sample ZMO-CNT/C. High-magnification XPS spectra of (b) Zn 2p, (c) Mn 2p, (d) C 1s, (e) N 1s, and (f) O 1s.

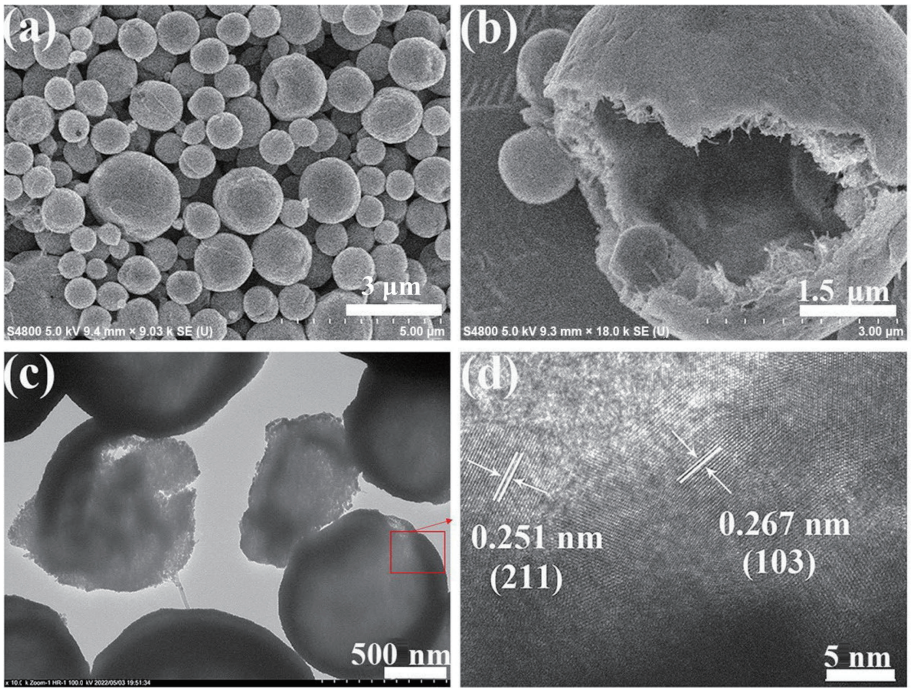

Figure 2 (a) Low- and (b) high-magnification SEM images of $ZnMn_2O_4$-CNT/C. (c) TEM and (d) HRTEM images of $ZnMn_2O_4$-CNT/C.

independent of the spheres were observed, indicating that the CNTs were well composited with the spheres. Figure 2(b) is a SEM image of a broken sphere, from which we can find that the sphere is a hollow structure. The CNTs in the walls of the spheres are clearly visible, and they are uniformly bound to the ZMO nanoparticles. The TEM image in Fig. 2(c) further confirms its hollow structure. Since the thickness of the wall is much larger than the diameter of the CNTs, only individual CNTs protruding outside the spherical wall can be found. The strong adsorption force of carbon nanotubes can effectively improve the electrochemical stability of the material. Figure 2(d) is the HRTEM image of ZMO-CNT/C, where the interplanar spacings of 0.251 and 0.267 nm correspond perfectly to the (211) and (103) planes of $ZnMn_2O_4$ (PDF#77-0470). Figure S3 in the ESM is the scanning TEM (STEM) and corresponding element mapping of the sample ZMO-CNT/C. The signals of Zn, Mn, O, C, and N elements overlap each other very well. Figure S4 in the ESM is the selected electron diffraction pattern of ZMO-CNT/C. It can be seen that it has a polycrystalline structure and good crystallinity, indicating that the ZMO nanoparticles are small in size and uniform in distribution. Furthermore, more extensive SEM and TEM images of different samples are shown in Figs. S5 and S6 in the ESM.

We also discussed the N_2 adsorption/desorption characteristics of the samples to obtain the BET specific surface area and BJH pore size distribution. Figure S7(a) in the ESM reveals that the specific surface areas of ZMO-CNT/C, ZMO/C, ZMO-CNT/C-400, and ZMO-CNT/C-500 are 81.867, 94.500, 56.386, and 21.942 $m^2 \cdot g^{-1}$, respectively, indicating that with the increase of calcination temperature, the specific surface area decreases. This is because with the increase of temperature, the grain size of ZMO increases, while the porosity of the microspheres decreases, so the specific surface area of the material decreases. It can be seen from Fig. S7(b) in the ESM that the pore size distribution of ZMO-CNT/C ranges from 2–30 nm, which is a typical mesoporous material. Part of the pore size is distributed in 3–4 nm and the other is distributed in 8–10 nm, this abundant pore structure facilitates the intercalation/extraction of zinc ions during charging and discharging.

The electrochemical performance of the sample ZMO-CNT/C hollow microspheres as zinc cathode was tested by cyclic voltammetry. As shown in Fig. 3(a), the initial periodic profile is slightly different from the later one. During subsequent cycles, the offset occurs due to kinetic changes. Two clearly overlapping oxidation peaks can be observed at 1.59 and 1.63 V after charging due to the detachment of zinc ions from the spinel $ZnMn_2O_4$ tetrahedral framework. In the subsequent cathodic scan, two reduction peaks appeared at 1.36 and 1.18 V, attributed to the stepwise electrochemical intercalation of Zn^{2+} [34]. At the same time, the continuous increase of redox current was observed, indicating that the electrode material was continuously activated, which was further confirmed in the subsequent galvanostatic charge–discharge tests. The charge–discharge curves of ZMO-CNT/C at 0.5 $A \cdot g^{-1}$ are shown in Fig. 3(b). No obvious discharge plateau was seen initially, and the plateau became more and more obvious with cycling. The discharge specific capacities at 50, 100, and 150 cycles were 282.95, 263.95, and 209.71 $mAh \cdot g^{-1}$, respectively. Its Coulombic efficiency remains above 99.00%, and the charge–discharge platform becomes more and more obvious, indicating that the material is continuously activated in the first few laps.

Figures 3(c) and 3(d) show the rate performance of products. It can be seen that the specific discharge capacities of ZMO-CNT/C are 449.97, 394.19, 281.28, 175.00, and 101.10 $mAh \cdot g^{-1}$ at current densities of 0.1, 0.2, 0.5, 1.0, and 2.0 $A \cdot g^{-1}$. Its reversible capacity reaches 362.56 $mAh \cdot g^{-1}$ when the current density is recovered from 2.0 $A \cdot g^{-1}$ to 0.2 $A \cdot g^{-1}$, indicating that ZMO-CNT/C has a good ability to withstand current changes. ZMO/C, ZMO-CNT/C-400, and ZMO-CNT/C-500 have similar trends, but the overall capacity is relatively low. Figure 3(e) shows the long cycle curves of each sample at a current density of 1.0 $A \cdot g^{-1}$. It can be seen that the capacity is very low at the beginning. Due to the continuous activation of the material with the continuous charging and discharging, there will be a phenomenon of continuous capacity growth. After that, the discharge specific capacity of ZMO-CNT/C fluctuates and decays slowly. However, the discharge specific capacity of ZMO/C, ZMO-CNT/C-400, and ZMO-CNT/C-500 showed a severe attenuation after 200 cycles. At this time, it can be seen that ZMO-CNT/C has the unique advantages of CNTs, and CNTs have high electrical conductivity. In addition, the CNTs have strong adsorption force to $ZnMn_2O_4$ nanoparticles and

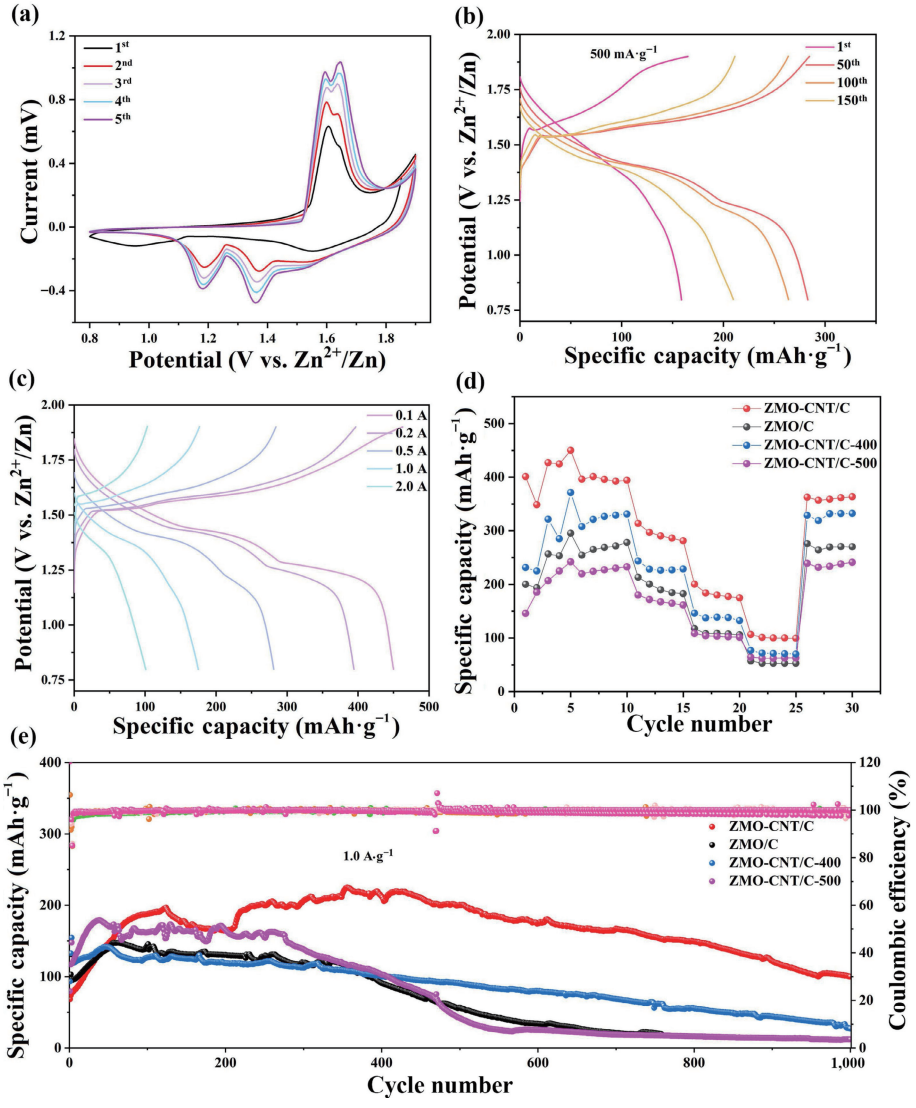

Figure 3 (a) CV curves of ZMO-CNT/C at a scan rate of 0.2 mV·s^{-1} between 0.8 and 1.9 V versus Zn/Zn^{2+}. (b) Charge/discharge curves of ZMO-CNT/C at a current density of 0.5 A·g^{-1}. (c) The charge–discharge curves of ZMO-CNT/C at 0.1–2.0 A·g^{-1}. (d) The rate performance of samples at various current densities from 0.1 to 2.0 A·g^{-1}, and (e) long-cycle performance test of samples at a current density of 1.0 A·g^{-1}.

under the synergistic effect of mesoporous hollow structure and cationic defects, provide long-term cycling stability of the material, thus exhibiting excellent zinc storage performance. Therefore, the discharge specific capacity of the sample ZMO-CNT/C after 1,000 cycles is 100.06 mAh·g^{-1}, while the discharge specific capacities of ZMO-CNT/C-400 and ZMO-CNT/C-500 are only 27.25 and 11.94 mAh·g^{-1}, respectively. After 750 cycles, the capacity of ZMO/C has dropped to 20.18 mAh·g^{-1}.

In order to further study the storage and reaction electrode mechanism of the sample ZMO-CNT/C, Fig. 4(a) shows the CV curves of ZMO-CNT/C at different scan rates. At scan rates of 0.1, 0.2, 0.3, 0.4, and 0.5 mV·s^{-1}, with the increase of scan rate, the peak current intensity increases continuously, the positions of the anodic and cathodic peaks change sequentially, and the width of the peaks also widens. The shape of the CV curve does not change significantly, indicating that the sample ZMO-CNT/C has a good rate capability. In addition, its CV curves at different scan rates were investigated for its electrochemical kinetic properties. The main oxidation and reduction peaks in Fig. 4(a) are labeled as 1, 2, 3, and 4, respectively. According to the formula of $\log i = \log a + b\log v$, the change of the current in the battery with the scan rate is analyzed, where i and v are the peak current and scan rate, and a and b are constants. The reaction kinetics can be analyzed by the b value. When the b value reaches about 0.5, the electrochemical reaction is mainly affected by ion diffusion. When the b value is closer to 1, the electrochemical reaction is affected by Faraday pseudocapacitance [35]. It can be seen from Fig. 4(b) that the slopes of peaks 1, 2, 3, and 4 are 0.572, 0.608, 0.607, and 0.747, respectively. This indicates that the electrochemical performance of ZMO-CNT/C materials is affected by both ion diffusion and Faraday pseudocapacitance. From Figs. 4(c) and 4(d), we can see the specific pseudocapacitance ratios at different scan speeds. The results show that the pseudocapacitance ratio increases with the scan speed and the pseudocapacitance ratio of ZMO-CNT/C at a scan speed of 0.5 mV·s^{-1} reaches 88.9%, indicating that the electrochemical kinetics are more affected by pseudocapacitance. The differences in Zn^{2+} de/intercalation kinetics in each sample were further analyzed by electrochemical impedance spectroscopy (EIS), in which ZMO-CNT/C had the lowest charge transfer resistance, mainly due to the high conductivity of CNTs. And the hollow mesoporous microsphere structure alleviates the volume expansion caused by the intercalation and intercalation of zinc ions, thus providing excellent cycling stability.

The kinetics of Zn^{2+} diffusion in ZMO-CNT/C cathodes were investigated by galvanostatic intermittent titration technique (GITT). The specific GITT experiment and calculation method are shown in Fig. S8 in the ESM, according to which the average D_{Zn} value of ZMO-CNT/C during discharge is 1.68×10^{-11} cm^2·s^{-1},

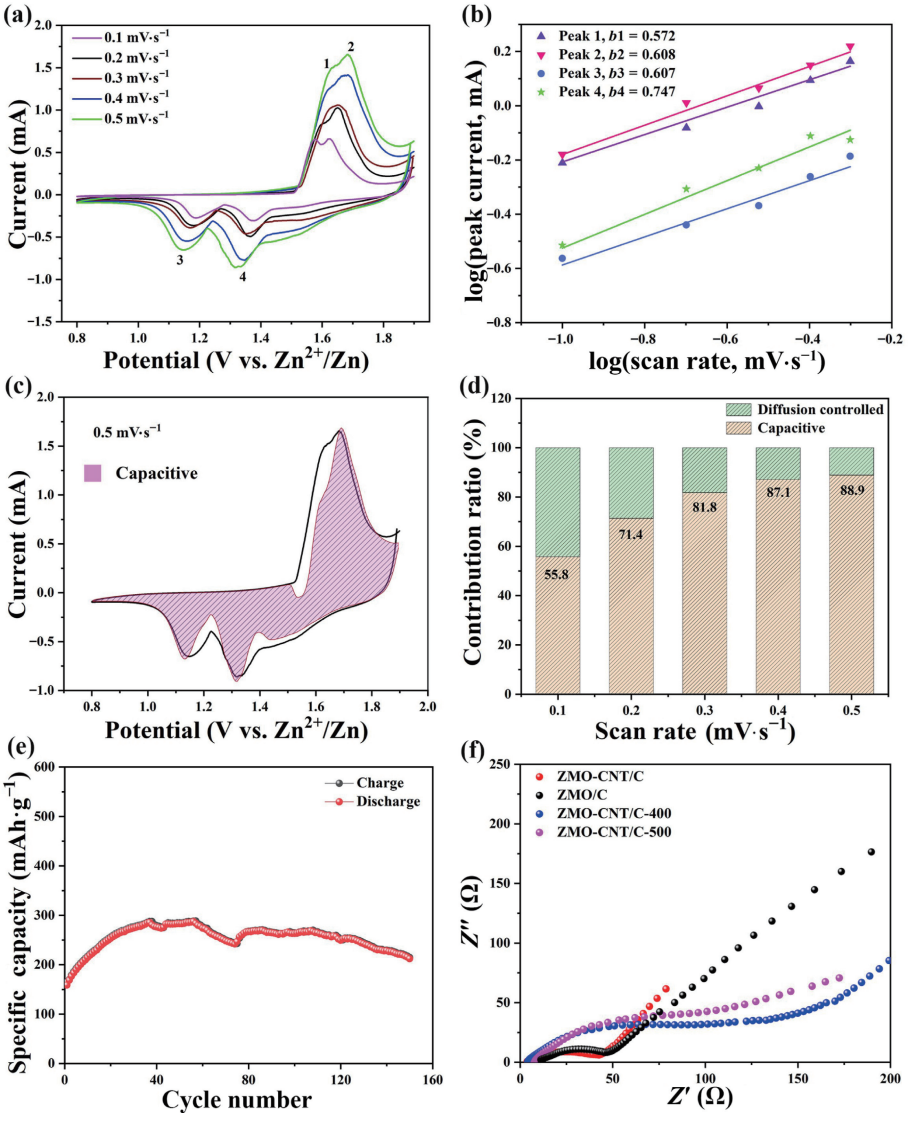

Figure 4 (a) CV curves of ZMO-CNT/C electrodes at different scan rates. (b) The corresponding log(peak current) versus log(scan rate) plots at each redox peak. (c) CV curve with a capacitive contribution at 0.5 mV·s^{-1}. (d) Capacitive contribution at various scan rates. (e) The cycling performance of ZMO-CNT/C at 0.5 A·g^{-1}, and (f) electrochemical impedance spectroscopy of the synthesized products after 10 cycles at a rate of 0.5 A·g^{-1}.

and the average D_{Zn} value during charge is 1.21 × 10^{-11} cm^2·s^{-1}, much larger than Zn^{2+} in spinel $ZnMn_2O_4$ [30]. It can be seen that the ZMO-CNT/C material is more conducive to the de-intercalation and insertion of zinc ions under the dual synergistic effect of CNTs and defect structures. In addition, ESM is available for more electrochemical performance tests of ZMO/C, ZMO-CNT/C-400, and ZMO-CNT/C-500 (Figs. S9–S11 in the ESM). Finally, the SEM test of the cycled ZMO-CNT/C was carried out. Figure S12 in the ESM shows that the material structure remains intact after long cycles. In addition, we compared the electrochemical performance of manganese-based oxides with those reported for AZIBs, which showed that the obtained unique structure has excellent zinc storage properties (Table S1 in the ESM).

4 Conclusions

In conclusion, we constructed hollow mesoporous $ZnMn_2O_4$ composite microspheres with carbon nanotubes embedded in the shells for AZIBs. Its hollow structure can effectively buffer the large volume change caused by ion intercalation and deintercalation, and its excellent mesoporosity provides more channels for zinc ion transport. In addition, the carbon nanotubes in the shell provide high electrical conductivity, and its strong adsorption force to $ZnMn_2O_4$ nanoparticles exists in synergy with cationic defects, which ensures the stability of the material under long-term cycles and provides excellent zinc storage performance. As expected, the obtained $ZnMn_2O_4$-CNT/C remains 209.71 mAh·g^{-1} after 150 cycles at a rate of 0.5 A·g^{-1} and still reserves a specific capacity of 100.06 mAh·g^{-1} at a rate of 1.0 A·g^{-1} after 1,000 cycles. This mesoporous hollow structure with interwoven carbon tubes in the shell improves the stability of the material and may have applications in other energy storage devices.

Acknowledgements

This work was supported by the National Natural Science Foundation of China (Nos. 21871005 and 22171005), the University Synergy Innovation Program of Anhui Province (Nos. GXXT-2020-005, GXXT-2021-012, and GXXT-2021-013), and Open project of Shanghai Institute of Technical Physics (No. IIMOKFJJ-19-09).

Electronic Supplementary Material: Supplementary material (additional FESEM, TEM, XRD, BET, TGA, SAED, GITT, cyclic performances, charge/discharge curves, and Table comparison of materials) is available in the online version of this article at

https://doi.org/10.1007/s12274-022-4772-x.

References

[1] Kundu, D.; Adams, B. D.; Duffort, V.; Vajargah, S. H.; Nazar, L. F. A high-capacity and long-life aqueous rechargeable zinc battery using a metal oxide intercalation cathode. *Nat. Energy* **2016**, *1*, 16119.

[2] Tong, Y. F.; Wang, X. H.; Zhang, Y.; Huang, W. W. Recent advances of covalent organic frameworks in lithium ion batteries. *Inorg. Chem. Front.* **2021**, *8*, 558–571.

[3] Liu, Z.; Pulletikurthi, G.; Endres, F. A prussian blue/zinc secondary battery with a bio-ionic liquid–water mixture as electrolyte. *ACS Appl. Mater. Interfaces* **2016**, *8*, 12158–12164.

[4] Li, H. F.; Han, C. P.; Huang, Y.; Huang, Y.; Zhu, M. S.; Pei, Z. X.; Xue, Q.; Wang, Z. F.; Liu, Z. X.; Tang, Z. J. et al. An extremely safe and wearable solid-state zinc ion battery based on a hierarchical structured polymer electrolyte. *Energy Environ. Sci.* **2018**, *11*, 941–951.

[5] Wan, F.; Zhang, L. L.; Dai, X.; Wang, X. Y.; Niu, Z. Q.; Chen, J. Aqueous rechargeable zinc/sodium vanadate batteries with enhanced performance from simultaneous insertion of dual carriers. *Nat. Commun.* **2018**, *9*, 1656.

[6] Ma, L. T.; Li, N.; Long, C. B.; Dong, B. B.; Fang, D. L.; Liu, Z. X.; Zhao, Y. W.; Li, X. L.; Fan, J.; Chen, S. M. et al. Achieving both high voltage and high capacity in aqueous zinc-ion battery for record high energy density. *Adv. Funct. Mater.* **2019**, *29*, 1906142.

[7] Li, G. L.; Yang, Z.; Jiang, Y.; Jin, C. H.; Huang, W.; Ding, X. L.; Huang, Y. H. Towards polyvalent ion batteries: A zinc-ion battery based on NASICON structured $Na_3V_2(PO_4)_3$. *Nano Energy* **2016**, *25*, 211–217.

[8] Qin, H. G.; Yang, Z. H.; Chen, L. L.; Chen, X.; Wang, L. M. A high-rate aqueous rechargeable zinc ion battery based on the VS_4@rGO nanocomposite. *J. Mater. Chem. A* **2018**, *6*, 23757–23765.

[9] Jia, D. D.; Zheng, K.; Song, M.; Tan, H.; Zhang, A. T.; Wang, L. H.; Yue, L. J.; Li, D.; Li, C. W.; Liu, J. Q. $VO_2{\cdot}0.2H_2O$ nanocuboids anchored onto graphene sheets as the cathode material for ultrahigh capacity aqueous zinc ion batteries. *Nano Res* **2020**, *13*, 215–224.

[10] Schmidt, O.; Hawkes, A.; Gambhir, A.; Staffell, I. The future cost of electrical energy storage based on experience rates. *Nat. Energy* **2017**, *2*, 17110.

[11] Du, Y. H.; Wang, X. Y.; Sun, J. C. Tunable oxygen vacancy concentration in vanadium oxide as mass-produced cathode for aqueous zinc-ion batteries. *Nano Res.* **2021**, *14*, 754–761.

[12] Li, C. G.; Zhang, X. D.; He, W.; Xu, G. G.; Sun, R. Cathode materials for rechargeable zinc-ion batteries: From synthesis to mechanism and applications. *J. Power Sources* **2020**, *449*, 227596.

[13] Ming, J.; Guo, J.; Xia, C.; Wang, W. X.; Alshareef, H. N. Zinc-ion batteries: Materials, mechanisms, and applications. *Mater. Sci. Eng. R Rep.* **2019**, *135*, 58–84.

[14] Liu, T. T.; Cheng, X.; Yu, H. X.; Zhu, H. J.; Peng, N.; Zheng, R. T.; Zhang, J. D.; Shui, M.; Cui, Y. H.; Shu, J. An overview and future perspectives of aqueous rechargeable polyvalent ion batteries. *Energy Storage Mater.* **2019**, *18*, 68–91.

[15] Zhou, Y.; Wang, C.; Chen, F. R.; Wang, T. J.; Ni, Y. Y.; Yu, N.; Geng, B. Y. Scalable fabrication of $NiCoMnO_4$ yolk–shell microspheres with gradient oxygen vacancies for high-performance aqueous zinc ion batteries. *J. Colloid Interface Sci.* **2022**, *626*, 314–323.

[16] Jia, H.; Wang, Z. Q.; Tawiah, B.; Wang, Y. D.; Chan, C. Y.; Fei, B.; Pan, F. Recent advances in zinc anodes for high-performance aqueous Zn-ion batteries. *Nano Energy* **2020**, *70*, 104523.

[17] Qin, L. P.; Zhu, Q.; Li, L. J.; Fang, G. Z.; Li, S. J.; Cheng, H.; Guo, W. M.; Gao, H. L. Improved electrochemical performance of $ZnMn_2O_4$/CuO composite as cathode materials for aqueous zinc-ion batteries. *Ionics* **2021**, *27*, 4783–4792.

[18] Yao, Z. F.; Cai, D. P.; Cui, Z. X.; Wang, Q. T.; Zhan, H. B. Strongly coupled zinc manganate nanodots and graphene composite as an advanced cathode material for aqueous zinc ion batteries. *Ceram. Int.* **2020**, *46*, 11237–11245.

[19] Wu, X. W.; Xiang, Y. H.; Peng, Q. J.; Wu, X. S.; Li, Y. H.; Tang, F.; Song, R. C.; Liu, Z. X.; He, Z. Q.; Wu, X. M. Green-low-cost rechargeable aqueous zinc-ion batteries using hollow porous spinel $ZnMn_2O_4$ as the cathode material. *J. Mater. Chem. A* **2017**, *5*, 17990–17997.

[20] Gao, F.; Mei, B.; Xu, X. Y.; Ren, J. H.; Zhao, D. C.; Zhang, Z.; Wang, Z. L.; Wu, Y. T.; Liu, X.; Zhang, Y. Rational design of $ZnMn_2O_4$ nanoparticles on carbon nanotubes for high-rate and durable aqueous zinc-ion batteries. *Chem. Eng. J.* **2022**, *448*, 137742.

[21] Sheng, J.; Zhu, S.; Jia, G. D.; Liu, X.; Li, Y. Carbon nanotube supported bifunctional electrocatalysts containing iron-nitrogen-carbon active sites for zinc-air batteries. *Nano Res.* **2021**, *14*, 4541–4547.

[22] Park, G. D.; Kim, J. H.; Park, S. K.; Kang, Y. C. $MoSe_2$ embedded CNT-reduced graphene oxide composite microsphere with superior sodium ion storage and electrocatalytic hydrogen evolution performances. *ACS Appl. Mater. Interfaces* **2017**, *9*, 10673–10683.

[23] Zeng, L. C.; Pan, F. S.; Li, W. H.; Jiang, Y.; Zhong, X. W.; Yu, Y. Free-standing porous carbon nanofibers-sulfur composite for flexible Li-S battery cathode. *Nanoscale* **2014**, *6*, 9579–9587.

[24] Shchegolkov, A. V.; Komarov, F. F.; Lipkin, M. S.; Milchanin, O. V.; Parfimovich, I. D.; Shchegolkov, A. V.; Semenkova, A. V.; Velichko, A. V.; Chebotov, K. D.; Nokhaeva, V. A. Synthesis and study of cathode materials based on carbon nanotubes for lithium-ion batteries. *Inorg. Mater.: Appl. Res.* **2021**, *12*, 1281–1287.

[25] Liu, Y. Z.; Chi, X. W.; Han, Q.; Du, Y. X.; Huang, J. Q.; Liu, Y.; Yang, J. H. α-MnO_2 nanofibers/carbon nanotubes hierarchically assembled microspheres: Approaching practical applications of high-performance aqueous Zn-ion batteries. *J. Power Sources* **2019**, *443*, 227244.

[26] Zhou, Y.; Wang, C.; Chen, F. R.; Wang, T. J.; Ni, Y. Y.; Sun, H. X.; Yu, N.; Geng, B. Y. Synchronous constructing ion channels and confined space of Co_3O_4 anode for high-performance lithium-ion batteries. *Nano Res.* **2022**, *15*, 6192–6199.

[27] Liu, Z.; Yu, M. K.; Wang, X. D.; Lai, F. Y.; Wang, C.; Yu, N.; Sun, H. X.; Geng, B. Y. Sandwich shelled TiO_2@Co_3O_4@Co_3O_4/C hollow spheres as anode materials for lithium ion batteries. *Chem. Commun.* **2021**, *57*, 1786–1789.

[28] Sun, H. X.; Du, H. R.; Yu, M. K.; Huang, K. F.; Yu, N.; Geng, B. Y. Vesicular $Li_3V_2(PO_4)_3$/C hollow mesoporous microspheres as an efficient cathode material for lithium-ion batteries. *Nano Res.* **2019**, *12*, 1937–1942.

[29] Su, L.; Gao, L. J.; Du, Q. H.; Hou, L. Y.; Yin, X. C.; Feng, M. Y.; Yang, W.; Ma, Z. P.; Shao, G. J. Formation of micron-sized nickel cobalt sulfide solid spheres with high tap density for enhancing pseudocapacitive properties. *ACS Sustainable Chem. Eng.* **2017**, *5*, 9945–9954.

[30] Zhang, N.; Cheng, F. Y.; Liu, Y. C.; Zhao, Q.; Lei, K. X.; Chen, C. C.; Liu, X. S.; Chen, J. Cation-deficient spinel $ZnMn_2O_4$ cathode in $Zn(CF_3SO_3)_2$ electrolyte for rechargeable aqueous Zn-ion battery. *J. Am. Chem. Soc.* **2016**, *138*, 12894–12901.

[31] Chen, L. L.; Yang, Z. H.; Qin, H. G.; Zeng, X.; Meng, J. L. Advanced electrochemical performance of $ZnMn_2O_4$/N-doped graphene hybrid as cathode material for zinc ion battery. *J. Power Sources* **2019**, *425*, 162–169.

[32] Chen, F. R.; Liu, Z.; Yu, N.; Sun, H. X.; Geng, B. Y. Constructing an interspace in MnO@NC microspheres for superior lithium ion battery anodes. *Chem. Commun.* **2021**, *57*, 10951–10954.

[33] Jiang, L.; Wu, Z. Y.; Wang, Y. A.; Tian, W. C.; Yi, Z. Y.; Cai, C. L.; Jiang, Y. C.; Hu, L. F. Ultrafast zinc-ion diffusion ability observed in 6.0-nanometer spinel nanodots. *ACS Nano* **2019**, *13*, 10376–10385.

[34] Pan, H. L.; Shao, Y. Y.; Yan, P. F.; Cheng, Y. W.; Han, K. S.; Nie, Z. M.; Wang, C. M.; Yang, J. H.; Li, X. L.; Bhattacharya, P. et al. Reversible aqueous zinc/manganese oxide energy storage from conversion reactions. *Nat. Energy* **2016**, *1*, 16039.

[35] Ma, S. C.; Sun, M.; Wang, S. X.; Li, D. S.; Liu, W. L.; Ren, M. M.; Kong, F. G.; Wang, S. J.; Xia, Y. M. Zinc manganate/manganic oxide bi-component nanorod as excellent cathode for zinc-ion battery. *Scripta Mater.* **2021**, *194*, 113707.